Rahman, F. M. Mahafugur; Riaz, Usama; Kukkola, Jarno; Routimo, Mikko; Hinkkanen, Marko

Observer-based current control for converters with an LCL filter

Published in:
IEEE 9th International Symposium on Sensorless Control for Electrical Drives, SLED 2018

DOI:
10.1109/SLED.2018.8486047

Published: 13/09/2018

Document Version
Peer reviewed version

Observer-Based Current Control for Converters With an LCL Filter: Robust Design for Weak Grids

F. M. Mahafugur Rahman*, Usama Riaz*, Jarno Kukkola*†, Mikko Routimo*†, and Marko Hinkkanen*
*Aalto University School of Electrical Engineering, Espoo, Finland
†ABB Drives, Helsinki, Finland

***Abstract*—This paper deals with state-feedback current control for power converters, which are equipped with an LCL filter and connected to a weak grid. The grid-side current is measured and other states needed by the current controller are estimated using a reduced-order observer. The control system is designed directly in the discrete-time domain. The gains of the control system are calculated using direct pole placement, assuming a strong grid. Recommendations for the nominal pole locations are given. The results show that the control system is robust against the unknown grid impedance, ranging from strong to very-weak grid conditions. The proposed design is validated by means of experiments.**

***Index Terms*—Grid converter, LCL filter, reduced-order observer, state-feedback current control, weak grid.**

I. Introduction

Grid converters are typically used to interface distributed and renewable energy sources with the AC grid. Long transmission lines increase the grid impedance seen from the point of common coupling (PCC). The large and unknown grid impedance may lead to unstable operation of a converter [1]–[4]. The grid impedance is related to the short-circuit ratio (SCR), which is the ratio of the short-circuit capacity of the AC system to the rated DC power [5]. The grid is categorized as weak if SCR < 3.

In order to connect a converter to the grid, an LCL filter is a preferred option to attenuate the switching harmonics because of its compact size [6], [7]. However, the LCL filter presents a resonant behavior that needs to be damped. The resonance of the LCL filter can be damped passively by introducing additional passive elements [8] or actively using control [6], [9], [10]. Active damping of the resonance is preferred since it makes the system more efficient than passive damping. However, the active damping of the LCL-filter resonance becomes more difficult due to the large grid impedance [10], [11].

The state-feedback current control provides a convenient and straightforward way for active resonance damping and for setting the desired dominant dynamics [6], [7], [12]–[15]. Using direct pole placement, the controller gains can be expressed analytically using the system parameters and the desired (nominal) pole locations, cf. [7], [13]. However, the actual poles of the system depend on the unknown grid impedance, which may degrade the dynamic performance and even cause the instability.

For the full-state feedback, all the states must be measured or estimated using an observer. The observer reduces the number of sensors, increases reliability, and decreases the costs in comparison with the methods in [7], [16]. The observer could be of full order [13], [17] or of reduced order [15], [18]. The reduced-order observer provides better disturbance rejection, but it is more sensitive to noise than the full-order observer [18].

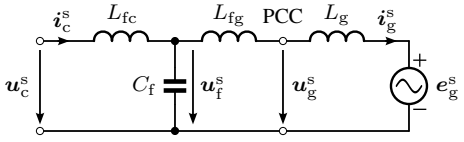

Fig. 1. Space-vector circuit model of an LCL filter and a grid in stationary coordinates (vectors marked with the superscript s).

The continuous-time design decreases the pole-placement accuracy with low sampling (switching) frequencies. The realized dynamics can be much worse than the desired dynamics, cf. [13]. The direct discrete-time design makes it possible to choose the sampling frequency more freely [13], [14]. In addition, the intrinsic delays of the digital implementation and pulse-width modulator (PWM) can be easily taken into account in the direct discrete-time design, giving superior performance as compared to the continuous-time design [13], [14].

This work deals with control of grid-connected converters equipped with an LCL filter, taking into account the weak-grid conditions. A state-feedback current controller is designed directly in the discrete-time domain. The grid-side current is measured and other states are estimated using a reduced-order observer. The design rules for robust operation against grid inductance variations are given. It is shown that stable operation from strong-grid conditions to very weak-grid conditions can be achieved without changing the tuning of the control system. The proposed design is experimentally evaluated using a 12.5-kVA grid converter.

II. System Model

A. Continuous-Time Model

Fig. 1 shows an equivalent circuit of an LCL filter connected to an inductive grid. The converter voltage is denoted by $\boldsymbol{u}_{\mathrm{c}}$, the voltage across the capacitor by $\boldsymbol{u}_{\mathrm{f}}$, the PCC voltage by $\boldsymbol{u}_{\mathrm{g}}$, and the grid voltage by $\boldsymbol{e}_{\mathrm{g}}$. The converter-side current is denoted by $\boldsymbol{i}_{\mathrm{c}}$ and the grid-side current by $\boldsymbol{i}_{\mathrm{g}}$. The LCL filter parameters are: converter-side inductance L_{fc}; capacitance C_{f};

TABLE I
PARAMETERS OF A 12.5-KVA CONVERTER SYSTEM

Parameter	Value	Value (p.u.)
LCL filter		
Capacitance C_f	8.8 μF	0.036
Converter-side inductance L_fc	3.3 mH	0.081
Grid-side inductance L_fg	3.0 mH	0.074
Grid		
Inductance L_g (strong grid)	0	0
Inductance L_g (very weak grid)	37 mH	0.926
Angular frequency ω_g	$2\pi\cdot$ 50 rad/s	1
Voltage (phase-neutral, peak)	$\sqrt{2/3}\cdot$ 400 V	1
Converter		
Rated current (peak)	$\sqrt{2}\cdot$ 18.3 A	1
DC-bus voltage u_dc	650 V	2
Sampling period T_s	125 μs	

and grid-side inductance L_fg. The total grid-side inductance is given by

$$L_\mathrm{s} = L_\mathrm{fg} + L_\mathrm{g} \tag{1}$$

where the grid inductance is L_g. Losses of the filter and the grid are neglected. The resonance angular frequency of the system

$$\omega_\mathrm{p} = \sqrt{\frac{L_\mathrm{fc}+L_\mathrm{s}}{L_\mathrm{fc}L_\mathrm{s}C_\mathrm{f}}} \tag{2}$$

depends on the grid inductance L_g via the total grid-side inductance L_s.

In synchronous *dq*-coordinates rotating at the grid angular frequency ω_g, the dynamics of the grid-side current are

$$\begin{aligned}\frac{\mathrm{d}\mathbf{x}}{\mathrm{d}t} &= \underbrace{\begin{bmatrix} -\mathrm{j}\omega_\mathrm{g} & -\frac{1}{L_\mathrm{fc}} & 0 \\ \frac{1}{C_\mathrm{f}} & -\mathrm{j}\omega_\mathrm{g} & -\frac{1}{C_\mathrm{f}} \\ 0 & \frac{1}{L_\mathrm{s}} & -\mathrm{j}\omega_\mathrm{g} \end{bmatrix}}_{\mathbf{A}} \mathbf{x} + \underbrace{\begin{bmatrix} \frac{1}{L_\mathrm{fc}} \\ 0 \\ 0 \end{bmatrix}}_{\mathbf{B}_\mathrm{c}} \boldsymbol{u}_\mathrm{c} + \underbrace{\begin{bmatrix} 0 \\ 0 \\ -\frac{1}{L_\mathrm{s}} \end{bmatrix}}_{\mathbf{B}_\mathrm{g}} \boldsymbol{e}_\mathrm{g} \\ \boldsymbol{i}_\mathrm{g} &= \underbrace{\begin{bmatrix} 0 & 0 & 1 \end{bmatrix}}_{\mathbf{C}_\mathrm{g}} \mathbf{x} \end{aligned} \tag{3}$$

where $\mathbf{x} = \left[\boldsymbol{i}_\mathrm{c}, \boldsymbol{u}_\mathrm{f}, \boldsymbol{i}_\mathrm{g}\right]^\mathrm{T}$ is the state vector.

B. Hold-Equivalent Discrete-Time Model

The plant model is converted to a hold-equivalent discrete-time model. The PWM is modeled as the zero-order hold (ZOH) in stationary coordinates. With the sampling period T_s and the discrete-time index k, the hold-equivalent discrete-time model is

$$\begin{aligned}\mathbf{x}(k+1) &= \mathbf{\Phi}\mathbf{x}(k) + \mathbf{\Gamma}_\mathrm{c}\boldsymbol{u}_\mathrm{c}(k) + \mathbf{\Gamma}_\mathrm{g}\boldsymbol{e}_\mathrm{g}(k) \\ \boldsymbol{i}_\mathrm{g}(k) &= \mathbf{C}_\mathrm{g}\mathbf{x}(k) \end{aligned} \tag{4}$$

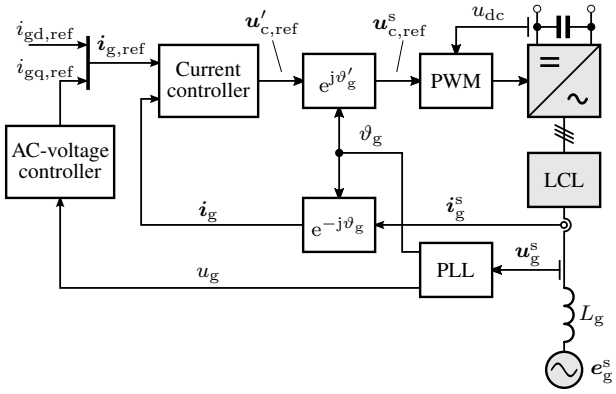

Fig. 2. Control system. The sampling is synchronized with the PWM. The PCC-voltage angle ϑ_g is obtained using a PLL. The effect of the computational delay on the voltage reference angle is compensated for in the coordinate transformation using $\vartheta'_\mathrm{g} = \vartheta_\mathrm{g} + T_\mathrm{s}\omega_\mathrm{g}$.

where the system matrices are

$$\begin{aligned}\mathbf{\Phi} &= \mathrm{e}^{\mathbf{A}T_\mathrm{s}} \qquad \mathbf{\Gamma}_\mathrm{c} = \left(\int_0^{T_\mathrm{s}} \mathrm{e}^{\mathbf{A}\tau}\mathrm{e}^{-\mathrm{j}\omega_\mathrm{g}(T_\mathrm{s}-\tau)}\mathrm{d}\tau\right)\mathbf{B}_\mathrm{c} \\ &\qquad\qquad \mathbf{\Gamma}_\mathrm{g} = \left(\int_0^{T_\mathrm{s}} \mathrm{e}^{\mathbf{A}\tau}\mathrm{d}\tau\right)\mathbf{B}_\mathrm{g}. \end{aligned} \tag{5}$$

The closed-form expressions of the matrices are given in [13].

C. System Parameters

The parameters of a 12.5-kVA converter system, given in Table I, will be used in this paper. Two different grid conditions are considered:

- Strong grid: $L_\mathrm{g} = 0$ (SCR $= 14$);
- Very weak grid: $L_\mathrm{g} = 0.926$ p.u. (SCR $= 1$).

The definition SCR $= 1/L_\mathrm{s}$ [p.u.], corresponding to [19], has been used, i.e., the SCR values are defined at the capacitor terminals of the LCL filter. Throughout the paper, the control system is tuned assuming $L_\mathrm{g} = 0$. Hence, the control system sees the grid inductance as a parameter error.

III. CURRENT CONTROL DESIGN

Fig. 2 shows the overall block diagram of the control system. The current controller operates in PCC-voltage coordinates, where $\boldsymbol{u}_\mathrm{g} = u_\mathrm{g} + \mathrm{j}0$. The grid-side current is measured for state-feedback control. The DC-link voltage u_dc is measured for the PWM and the PCC voltage is measured for the phase-locked loop (PLL) and for the AC-voltage controller.

Fig. 3 shows the observer-based current controller in more detail. Based on the separation principle [18], the control design procedure is divided into two steps: 1) full-state feedback control is designed assuming all the states are available; 2) reduced-order observer is designed separately.

A. Full-State Feedback Control

One-sampling-period computational delay exists in standard implementations. In stationary coordinates, the effect of the computational delay on the voltage production can be modeled

as $\boldsymbol{u}_{\mathrm{c}}^{\mathrm{s}}(k) = \boldsymbol{u}_{\mathrm{c,ref}}^{\mathrm{s}}(k-1)$, where $\boldsymbol{u}_{\mathrm{c,ref}}^{\mathrm{s}}$ is the voltage reference for the PWM according to Fig. 2. Transforming this expression to synchronous coordinates yields [13]

$$\boldsymbol{u}_{\mathrm{c}}(k) = \mathrm{e}^{-\mathrm{j}\omega_{\mathrm{g}}T_{\mathrm{s}}}\boldsymbol{u}_{\mathrm{c,ref}}(k-1) = \boldsymbol{u}'_{\mathrm{c,ref}}(k-1) \tag{6}$$

where the modified voltage reference $\boldsymbol{u}'_{\mathrm{c,ref}}$ is defined to simplify notation. The effect of the computational delay on the angle of the converter voltage is compensated for in the coordinate transformation, cf. Fig. 2. The extra state needed for modeling the computational delay is included in (4) as

$$\begin{aligned}\mathbf{x}_{\mathrm{d}}(k+1) &= \underbrace{\begin{bmatrix}\boldsymbol{\Phi} & \boldsymbol{\Gamma}_{\mathrm{c}}\\ \mathbf{0} & 0\end{bmatrix}}_{\boldsymbol{\Phi}_{\mathrm{d}}}\mathbf{x}_{\mathrm{d}}(k) + \underbrace{\begin{bmatrix}\mathbf{0}\\ 1\end{bmatrix}}_{\boldsymbol{\Gamma}_{\mathrm{cd}}}\boldsymbol{u}'_{\mathrm{c,ref}}(k) + \underbrace{\begin{bmatrix}\boldsymbol{\Gamma}_{\mathrm{g}}\\ 0\end{bmatrix}}_{\boldsymbol{\Gamma}_{\mathrm{gd}}}\boldsymbol{e}_{\mathrm{g}}(k)\\ \boldsymbol{i}_{\mathrm{g}}(k) &= \underbrace{\begin{bmatrix}\mathbf{C}_{\mathrm{g}} & 0\end{bmatrix}}_{\mathbf{C}_{\mathrm{gd}}}\mathbf{x}_{\mathrm{d}}(k)\end{aligned} \tag{7}$$

where $\mathbf{x}_{\mathrm{d}} = [\boldsymbol{i}_{\mathrm{c}}, \boldsymbol{u}_{\mathrm{f}}, \boldsymbol{i}_{\mathrm{g}}, \boldsymbol{u}_{\mathrm{c}}]^{\mathrm{T}}$ is the new state vector augmented with the delayed voltage reference.

For improved disturbance rejection, the system model (7) is also augmented with an integral state

$$\boldsymbol{x}_{\mathrm{i}}(k+1) = \boldsymbol{x}_{\mathrm{i}}(k) + \boldsymbol{i}_{\mathrm{g,ref}}(k) - \boldsymbol{i}_{\mathrm{g}}(k) \tag{8}$$

where $\boldsymbol{i}_{\mathrm{g,ref}}$ is the current reference. The augmented model is

$$\begin{aligned}\underbrace{\begin{bmatrix}\mathbf{x}_{\mathrm{d}}(k+1)\\ \boldsymbol{x}_{\mathrm{i}}(k+1)\end{bmatrix}}_{\mathbf{x}_{\mathrm{a}}(k+1)} &= \underbrace{\begin{bmatrix}\boldsymbol{\Phi}_{\mathrm{d}} & \mathbf{0}\\ -\mathbf{C}_{\mathrm{gd}} & 1\end{bmatrix}}_{\boldsymbol{\Phi}_{\mathrm{a}}}\underbrace{\begin{bmatrix}\mathbf{x}_{\mathrm{d}}(k)\\ \boldsymbol{x}_{\mathrm{i}}(k)\end{bmatrix}}_{\mathbf{x}_{\mathrm{a}}(k)} + \underbrace{\begin{bmatrix}\boldsymbol{\Gamma}_{\mathrm{cd}}\\ 0\end{bmatrix}}_{\boldsymbol{\Gamma}_{\mathrm{ca}}}\boldsymbol{u}'_{\mathrm{c,ref}}(k)\\ &\quad + \underbrace{\begin{bmatrix}\mathbf{0}\\ 1\end{bmatrix}}_{\boldsymbol{\Gamma}_{\mathrm{t}}}\boldsymbol{i}_{\mathrm{g,ref}}(k) + \underbrace{\begin{bmatrix}\boldsymbol{\Gamma}_{\mathrm{gd}}\\ 0\end{bmatrix}}_{\boldsymbol{\Gamma}_{\mathrm{ga}}}\boldsymbol{e}_{\mathrm{g}}(k)\\ \boldsymbol{i}_{\mathrm{g}}(k) &= \underbrace{\begin{bmatrix}\mathbf{C}_{\mathrm{gd}} & 0\end{bmatrix}}_{\mathbf{C}_{\mathrm{ga}}}\mathbf{x}_{\mathrm{a}}(k)\end{aligned} \tag{9}$$

where $\mathbf{x}_{\mathrm{a}}$ is the augmented state vector and $\boldsymbol{\Phi}_{\mathrm{a}}$, $\boldsymbol{\Gamma}_{\mathrm{ca}}$, $\boldsymbol{\Gamma}_{\mathrm{t}}$, and $\boldsymbol{\Gamma}_{\mathrm{ga}}$, and $\mathbf{C}_{\mathrm{ga}}$ are the augmented system matrices.

The reference feedforward is used for improved reference-tracking performance. In accordance with Fig. 3, the control law is

$$\boldsymbol{u}'_{\mathrm{c,ref}}(k) = \boldsymbol{k}_{\mathrm{t}}\boldsymbol{i}_{\mathrm{g,ref}}(k) + \boldsymbol{k}_{\mathrm{i}}\boldsymbol{x}_{\mathrm{i}}(k) - \mathbf{K}\mathbf{x}_{\mathrm{d}}(k) \tag{10}$$

where $\boldsymbol{k}_{\mathrm{t}}$ is the feedforward gain, $\boldsymbol{k}_{\mathrm{i}}$ is the integral gain, and $\mathbf{K} = \begin{bmatrix}\boldsymbol{k}_1, \boldsymbol{k}_2, \boldsymbol{k}_3, \boldsymbol{k}_4\end{bmatrix}$ is the state-feedback gain. From (9) and (10), the closed-loop reference-tracking transfer function is

$$\frac{\boldsymbol{i}_{\mathrm{g}}(z)}{\boldsymbol{i}_{\mathrm{g,ref}}(z)} = \mathbf{C}_{\mathrm{ga}}(z\mathbf{I} - \boldsymbol{\Phi}_{\mathrm{a}} + \boldsymbol{\Gamma}_{\mathrm{ca}}\mathbf{K}_{\mathrm{a}})^{-1}(\boldsymbol{k}_{\mathrm{t}}\boldsymbol{\Gamma}_{\mathrm{ca}} + \boldsymbol{\Gamma}_{\mathrm{t}}) \tag{11}$$

where $\mathbf{K}_{\mathrm{a}} = \begin{bmatrix}\mathbf{K}, -\boldsymbol{k}_{\mathrm{i}}\end{bmatrix}$ is the augmented state-feedback gain. The characteristic polynomial is

$$\boldsymbol{D}(z) = \det(z\mathbf{I} - \boldsymbol{\Phi}_{\mathrm{a}} + \boldsymbol{\Gamma}_{\mathrm{ca}}\mathbf{K}_{\mathrm{a}}). \tag{12}$$

Let the desired closed-loop characteristic polynomial be

$$\boldsymbol{D}(z) = (z - \boldsymbol{p}_1)(z - \boldsymbol{p}_2)(z - \boldsymbol{p}_3)(z - \boldsymbol{p}_4)(z - \boldsymbol{p}_5). \tag{13}$$

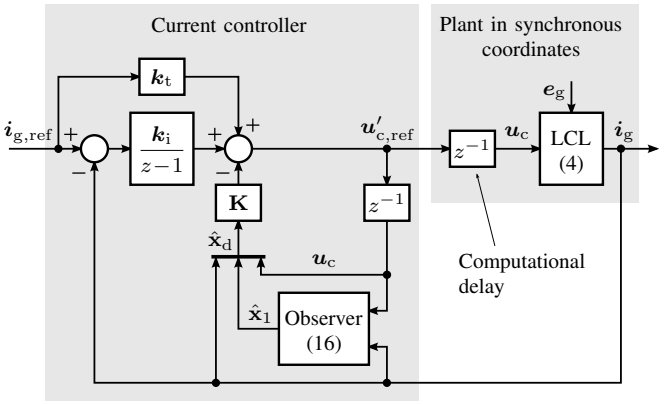

Fig. 3. State-feedback current control with a reduced-order observer. The true state $\mathbf{x}_{\mathrm{d}}$ in (10) is replaced with the state estimate $\hat{\mathbf{x}}_{\mathrm{d}}$.

The gain $\mathbf{K}_{\mathrm{a}}$ can be solved from (12) and (13) either analytically, as in [13], or using numerical tools.

The reference feedforward of the control system produces a zero in the closed-loop transfer function (11). If the reference-feedforward zero is to be placed at $\boldsymbol{z}_{\mathrm{t}}$, the feedforward gain becomes

$$\boldsymbol{k}_{\mathrm{t}} = \boldsymbol{k}_{\mathrm{i}}/(1 - \boldsymbol{z}_{\mathrm{t}}). \tag{14}$$

The reference-feedforward zero can be used to cancel one of the control poles.

B. Reduced-Order Observer

The presented scheme measures only the grid-side current $\boldsymbol{i}_{\mathrm{g}}$, cf. Fig. 3. To design the reduced-order observer, the state vector $\mathbf{x}(k)$ is split into the unknown states $\mathbf{x}_1(k)$ and the measured state $\boldsymbol{i}_{\mathrm{g}}(k)$. The grid voltage is considered as an unknown disturbance. The model (4) becomes

$$\begin{bmatrix}\mathbf{x}_1(k+1)\\ \boldsymbol{i}_{\mathrm{g}}(k+1)\end{bmatrix} = \begin{bmatrix}\boldsymbol{\Phi}_{11} & \boldsymbol{\Phi}_{12}\\ \boldsymbol{\Phi}_{21} & \boldsymbol{\phi}_{22}\end{bmatrix}\begin{bmatrix}\mathbf{x}_1(k)\\ \boldsymbol{i}_{\mathrm{g}}(k)\end{bmatrix} + \begin{bmatrix}\boldsymbol{\Gamma}_{\mathrm{c1}}\\ \boldsymbol{\gamma}_{\mathrm{c2}}\end{bmatrix}\boldsymbol{u}_{\mathrm{c}}(k) \tag{15}$$

where $\boldsymbol{\Phi}_{11}$, $\boldsymbol{\Phi}_{12}$, $\boldsymbol{\Phi}_{21}$, and $\boldsymbol{\phi}_{22}$ are submatrices of $\boldsymbol{\Phi}$ and $\boldsymbol{\Gamma}_{\mathrm{c1}}$ and $\boldsymbol{\gamma}_{\mathrm{c2}}$ are submatrices of $\boldsymbol{\Gamma}_{\mathrm{c}}$. Only the two unknown states $\mathbf{x}_1 = [\boldsymbol{i}_{\mathrm{c}}, \boldsymbol{u}_{\mathrm{f}}]^{\mathrm{T}}$ are to be estimated. Therefore, the reduced-order observer is formulated as [18]

$$\begin{aligned}\hat{\mathbf{x}}_1(k) &= \boldsymbol{\Phi}_{11}\hat{\mathbf{x}}_1(k-1) + \boldsymbol{\Phi}_{12}\boldsymbol{i}_{\mathrm{g}}(k-1) + \boldsymbol{\Gamma}_{\mathrm{c1}}\boldsymbol{u}_{\mathrm{c}}(k-1)\\ &\quad + \mathbf{K}_{\mathrm{o}}[\boldsymbol{i}_{\mathrm{g}}(k) - \boldsymbol{\phi}_{22}\boldsymbol{i}_{\mathrm{g}}(k-1)\\ &\quad - \boldsymbol{\gamma}_{\mathrm{c2}}\boldsymbol{u}_{\mathrm{c}}(k-1) - \boldsymbol{\Phi}_{21}\hat{\mathbf{x}}_1(k-1)]\end{aligned} \tag{16}$$

where $\mathbf{K}_{\mathrm{o}} = \begin{bmatrix}\boldsymbol{k}_{\mathrm{o1}}, \boldsymbol{k}_{\mathrm{o2}}\end{bmatrix}^{\mathrm{T}}$ is the observer gain. The characteristic polynomial of the estimation-error dynamics is

$$\boldsymbol{D}_{\mathrm{o}}(z) = \det(z\mathbf{I} - \boldsymbol{\Phi}_{11} + \mathbf{K}_{\mathrm{o}}\boldsymbol{\Phi}_{21}). \tag{17}$$

Let the desired observer characteristic polynomial be

$$\boldsymbol{D}_{\mathrm{o}}(z) = (z - \boldsymbol{p}_{\mathrm{o1}})(z - \boldsymbol{p}_{\mathrm{o2}}). \tag{18}$$

The gain $\mathbf{K}_{\mathrm{o}}$ is solved from (17) and (18).

It is worth noticing that the whole control system is comparatively simple: first the state estimate is updated using (16) and then the voltage reference is calculated using the control

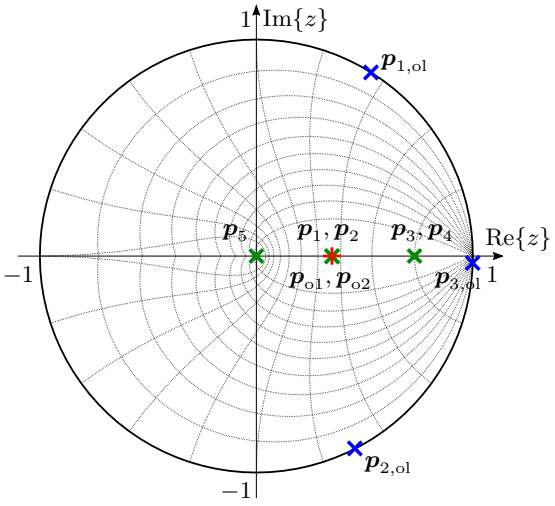

Fig. 4. Nominal pole locations at $L_\mathrm{g} = 0$: open-loop system (blue); control (green); observer (red). The parameters are: $\alpha_\mathrm{c} = 2\pi \cdot 400$ rad/s and $\zeta_\mathrm{r} = \zeta_\mathrm{o} = 1$.

law (10). The closed-form expressions are available both for the system matrices and for the gains.

C. Selection of Nominal Closed-Loop Poles

As shown in Fig. 4, the open-loop system (4) has three poles located at

$$\boldsymbol{p}_{1,2,\mathrm{ol}} = \exp[-\mathrm{j}(\omega_\mathrm{g} \pm \omega_\mathrm{p})T_\mathrm{s}] \qquad \boldsymbol{p}_{3,\mathrm{ol}} = \exp(-\mathrm{j}\omega_\mathrm{g}T_\mathrm{s}). \tag{19}$$

The computational delay and the integral action add two more poles. All the five closed-loop poles can be arbitrarily placed by means of full-state feedback. Based on the separation principle, the control and observer poles can be considered separately. The desired pole locations are discussed in the following.

1) Control Poles: To simplify the tuning process, the desired control pole locations are parametrized here as [13]

$$\begin{aligned} \boldsymbol{p}_{1,2} &= \exp\left[\left(-\zeta_\mathrm{r} \pm \mathrm{j}\sqrt{1-\zeta_\mathrm{r}^2}\right)\omega_\mathrm{p}T_\mathrm{s}\right] \\ \boldsymbol{p}_{3,4} &= \exp(-\alpha_\mathrm{c}T_\mathrm{s}) \\ \boldsymbol{p}_5 &= 0 \end{aligned} \tag{20}$$

where ζ_r and α_c are the design parameters. The undamped natural frequency ω_p of the resonant pole pair is not altered, but the damping ratio ζ_r can be set freely. The dominant dynamics are determined by the pair $\boldsymbol{p}_{3,4}$ of double real poles. The design parameter α_c corresponds to the approximate closed-loop bandwidth. The pole $\boldsymbol{p}_5$ originating from the computational delay is not moved since it is already in the optimal location. Fig. 4 shows the resulting control poles for $\zeta_\mathrm{r} = 1$, giving a critically-damped system in nominal conditions. The selection of ζ_r will be considered in more detail in Section IV.

The reference-feedforward zero is placed at

$$\boldsymbol{z}_\mathrm{t} = \exp(-\alpha_\mathrm{c}T_\mathrm{s}). \tag{21}$$

Therefore, it cancels one of the control poles at $\boldsymbol{p}_{3,4}$.

2) Observer Poles: The observer poles should preferably be placed at frequencies higher than the frequency of the dominant control poles [18]. The observer pole locations are parametrized as

$$\boldsymbol{p}_{\mathrm{o}1,\mathrm{o}2} = \exp\left[\left(-\zeta_\mathrm{o} \pm \mathrm{j}\sqrt{1-\zeta_\mathrm{o}^2}\right)\omega_\mathrm{p}T_\mathrm{s}\right] \tag{22}$$

where the damping ratio ζ_o is the design parameter. Fig. 4 shows the resulting poles for $\zeta_\mathrm{o} = 1$, giving a pair of real poles at the same location as $\boldsymbol{p}_{1,2}$.

IV. Robustness Analysis

The robustness of the observer-based current controller is examined by calculating the eigenvalues of the closed-loop system. The system shown in Fig. 3 is assumed, i.e., the outer control loops are not taken into account. The parameters are given in Table I.

Three parameters are needed for tuning the current controller: α_c, ζ_r, and ζ_o. The control system is tuned assuming the strong grid, i.e., $L_\mathrm{g} = 0$, which naturally means that the actual closed-loop poles will move from their nominal locations for any nonzero grid inductance L_g. In the following, the stability of the control system is studied taking into account nonzero L_g.

The following design parameters are first used: $\alpha_\mathrm{c} = 2\pi{\cdot}400$ rad/s and $\zeta_\mathrm{r} = \zeta_\mathrm{o} = 1$. Fig. 5(a) shows the loci of the closed-loop poles as the grid-side inductance is increased in the range $L_\mathrm{g} = 0 \ldots 0.926$ p.u., corresponding to the total grid-side inductance in the range $L_\mathrm{s} = L_\mathrm{fg} \ldots 1$ p.u. The green crosses show the nominal pole locations, i.e. $L_\mathrm{g} = 0$, corresponding to Fig. 4. When the grid inductance increases, the poles move toward the unit circle. The red crosses show the pole locations for the very-weak-grid case, i.e., $L_\mathrm{s} = 1$ p.u. All the poles are still inside the unit circle, i.e., the system is stable from nominal conditions to very-weak-grid conditions. The analysis was repeated with different values for the nominal bandwidth α_c while $\zeta_\mathrm{r} = \zeta_\mathrm{o} = 1$; it was found out that the poles are inside the unit circle if $\alpha_\mathrm{c} \geq 2\pi \cdot 46$ rad/s.

Fig. 5(b) shows the loci of the closed-loop poles for the very-weak-grid case ($L_\mathrm{s} = 1$ p.u.), when the damping ratios $\zeta_\mathrm{r} = \zeta_\mathrm{o}$ are varied from 0 to 1. The system is stable if $\zeta_\mathrm{r} = \zeta_\mathrm{o} > 0.22$. If the damping ratios are selected separately, stability condition changes. For example, if $\zeta_\mathrm{r} = 1$ is selected, $\zeta_\mathrm{o} \geq 0$ provides stable operation. In this paper, the damping ratios $\zeta_\mathrm{r} = \zeta_\mathrm{o} = 1$ are selected.

V. Implementation Aspects

A. Current Reference

The reference for the active-power-producing current component is

$$i_{\mathrm{gd,ref}} = \frac{2}{3}\frac{P_\mathrm{ref}}{u_{\mathrm{g,ref}}} \tag{23}$$

where $u_{\mathrm{g,ref}}$ is the reference for the PCC voltage and P_ref is the reference for the active power.

An AC-voltage controller is necessary for operation in weak grids [1], [4]. Here, an integral controller is used for simplicity.

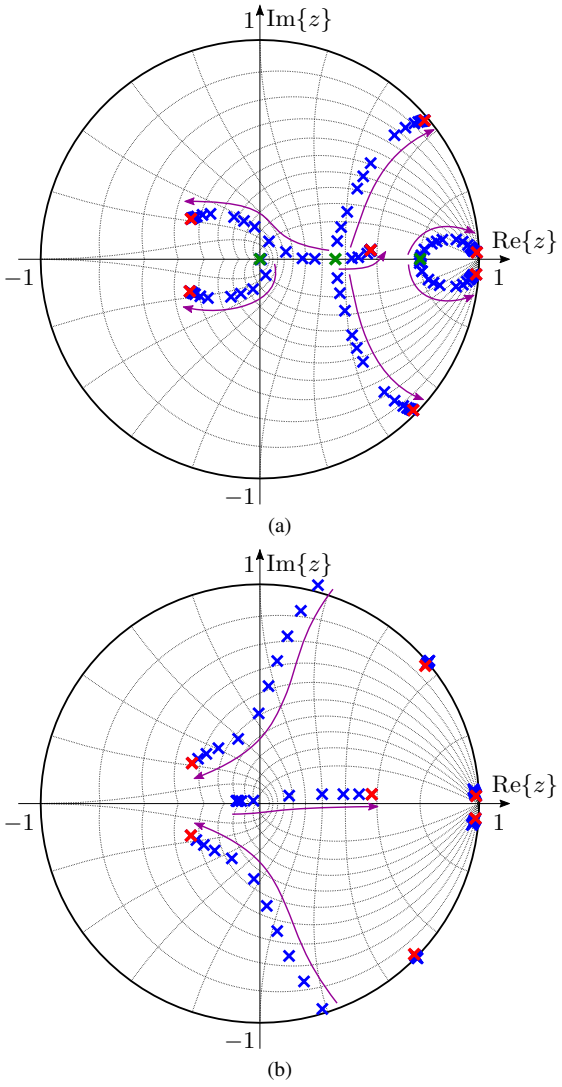

Fig. 5. Loci of the closed-loop poles: (a) total grid-side inductance is increased in the range $L_\mathrm{s} = L_\mathrm{fg} \ldots 1$ p.u. while $\zeta_\mathrm{r} = \zeta_\mathrm{o} = 1$; (b) nominal damping ratios are increased in the range $\zeta_\mathrm{r} = \zeta_\mathrm{o} = 0 \ldots 1$ while $L_\mathrm{s} = 1$ p.u. The nominal bandwidth is $\alpha_\mathrm{c} = 2\pi \cdot 400$ rad/s in both cases.

It gives the reference for the reactive-power-producing current component

$$i_{\mathrm{gq,ref}}(k) = \frac{T_\mathrm{s} k_{\mathrm{i,ac}}}{z-1} \left[u_{\mathrm{g,ref}}(k) - u_\mathrm{g}(k) \right] \tag{24}$$

where $k_{\mathrm{i,ac}}$ is the integral gain. The gain can be related to the approximate bandwidth α_{ac} of the AC-voltage control loop by means of a simple small-signal model, where the PLL dynamics are omitted and ideal current control is assumed. These assumptions lead to $k_{\mathrm{i,ac}} = \alpha_{\mathrm{ac}}/(\omega_\mathrm{g} L_\mathrm{B})$, where L_B is the base inductance.

B. PLL

A simple PLL operating in synchronous coordinates is used [20]. In weak grids, the PCC voltage varies with the grid current. Therefore, a slow PLL should be used in order to avoid the coupling between the current control dynamics and the PLL dynamics [2].

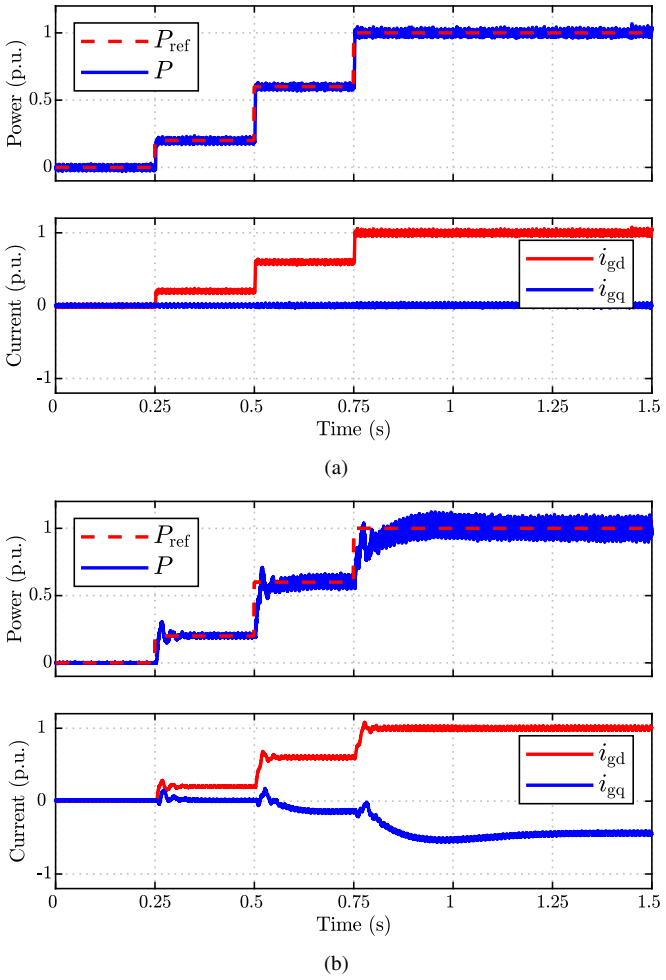

Fig. 6. Measured step responses of the active power and the corresponding grid-side current components i_gd and i_gq: (a) strong grid, $L_\mathrm{g} \approx 0$; (b) very weak grid, $L_\mathrm{s} \approx 1$ p.u. The same controller tuning based on $L_\mathrm{g} = 0$ is used in both cases.

VI. Experimental Results

The proposed control strategy is verified by means of experiments. A 12.5-kVA 50-Hz grid-connected converter is considered (Table I). The control method was implemented on the dSPACE DS1006 processor board. The switching frequency of the converter is 4 kHz and synchronous sampling (twice per carrier) is used. The bandwidth of the AC-voltage controller is $\alpha_{\mathrm{ac}} = 2\pi \cdot 10$ rad/s and the bandwidth of the PLL is $2\pi \cdot 2$ rad/s. The PCC voltage reference is $u_{\mathrm{g,ref}} = 1$ p.u. The design parameters of the current controller are $\alpha_\mathrm{c} = 2\pi \cdot 400$ rad/s and $\zeta_\mathrm{r} = \zeta_\mathrm{o} = 1$. The grid inductance $L_\mathrm{g} = 0$ is assumed in the control system.

Fig. 6(a) shows the measured active power response and the corresponding grid-side current components i_gd and i_gq in the strong-grid condition, when the active power reference P_ref is set with three successive steps ($0.2 \rightarrow 0.6 \rightarrow 1$ p.u.). As expected, the response in this nominal case is critically

damped. Under these conditions, the bandwidth α_c and the sampling frequency could be freely chosen within the limits coming from the Nyquist frequency and parameter accuracy.

Fig. 6(b) shows the measured active power response and the corresponding grid-side current components i_{gd} and i_{gq} in the very-weak-grid condition. It is worth mentioning that reactive current is needed in order to keep the PCC voltage at 1 p.u. It can be seen that the system remains stable even if the SCR ≈ 1. The same control system and parameters are used in both cases.

VII. Conclusion

This paper presented a state-feedback current controller with a reduced-order observer designed directly in the discrete-time domain for a grid converter equipped with an LCL filter. Only the grid-side current is measured for the current controller. The control method does not require additional damping for the resonance of the LCL filter. The controller provides stable operation in the whole range of grid inductance variation from strong-grid conditions to very weak-grid conditions. The design rules for the robust operation against the grid-impedance variations are given. The proposed method is validated by means of experiments.

Acknowledgment

The authors gratefully acknowledge ABB Oy, the Finnish Foundation for Technology Promotion, and the Walter Ahlström Foundation for the financial support.

References

[1] N. P. W. Strachan and D. Jovcic, "Stability of a variable-speed permanent magnet wind generator with weak AC grids," *IEEE Trans. Power Del.*, vol. 25, no. 4, pp. 2779–2788, Oct. 2010.

[2] J. Z. Zhou, H. Ding, S. Fan, Y. Zhang, and A. M. Gole, "Impact of short-circuit ratio and phase-locked-loop parameters on the small-signal behavior of a VSC-HVDC converter," *IEEE Trans. Power Del.*, vol. 29, no. 5, pp. 2287–2296, Oct. 2014.

[3] A. Egea-Alvarez, S. Fekriasl, F. Hassan, and O. Gomis-Bellmunt, "Advanced vector control for voltage source converters connected to weak grids," *IEEE Trans. Power Syst.*, vol. 30, no. 6, pp. 3072–3081, Nov. 2015.

[4] M. F. M. Arani and Y. A. R. I. Mohamed, "Analysis and performance enhancement of vector-controlled VSC in HVDC links connected to very weak grids," *IEEE Trans. Power Syst.*, vol. 32, no. 1, pp. 684–693, Jan. 2017.

[5] "IEEE guide for planning DC links terminating at AC locations having low short-circuit capacities," *IEEE Std. 1204-1997*, pp. 1–216, Jan. 1997.

[6] I. J. Gabe, V. F. Montagner, and H. Pinheiro, "Design and implementation of a robust current controller for VSI connected to the grid through an LCL filter," *IEEE Trans. Power Electron.*, vol. 24, no. 6, pp. 1444–1452, Jun. 2009.

[7] J. Dannehl, F. W. Fuchs, and P. B. Thøgersen, "PI state space current control of grid-connected PWM converters with LCL filters," *IEEE Trans. Power Electron.*, vol. 25, no. 9, pp. 2320–2330, Sept. 2010.

[8] R. Peña-Alzola, M. Liserre, F. Blaabjerg, R. Sebastián, J. Dannehl, and F. W. Fuchs, "Analysis of the passive damping losses in LCL-filter-based grid converters," *IEEE Trans. Power Electron.*, vol. 28, no. 6, pp. 2642–2646, Jun. 2013.

[9] Z. Xin, X. Wang, P. C. Loh, and F. Blaabjerg, "Grid-current-feedback control for LCL-filtered grid converters with enhanced stability," *IEEE Trans. Power Electron.*, vol. 32, no. 4, pp. 3216–3228, Apr. 2017.

[10] M. Liserre, R. Teodorescu, and F. Blaabjerg, "Stability of photovoltaic and wind turbine grid-connected inverters for a large set of grid impedance values," *IEEE Trans. Power Electron.*, vol. 21, no. 1, pp. 263–272, Jan. 2006.

[11] D. Pan, X. Ruan, C. Bao, W. Li, and X. Wang, "Capacitor-current-feedback active damping with reduced computation delay for improving robustness of LCL-type grid-connected inverter," *IEEE Trans. Power Electron.*, vol. 29, no. 7, pp. 3414–3427, Jul. 2014.

[12] M. H. Hedayati, A. Acharya B., and V. John, "Common-mode and differential-mode active damping for PWM rectifiers," *IEEE Trans. Power Electron.*, vol. 29, no. 6, pp. 3188–3200, Jun. 2014.

[13] J. Kukkola, M. Hinkkanen, and K. Zenger, "Observer-based state-space current controller for a grid converter equipped with an LCL filter: Analytical method for direct discrete-time design," *IEEE Trans. Ind. Appl.*, vol. 51, no. 5, pp. 4079–4090, Sept. 2015.

[14] R. Turner, S. Walton, and R. Duke, "Robust high-performance inverter control using discrete direct-design pole placement," *IEEE Trans. Ind. Electron.*, vol. 58, no. 1, pp. 348–357, Jan. 2011.

[15] D. Pérez-Estévez, J. Doval-Gandoy, A. G. Yepes, and O. López, "Positive- and negative-sequence current controller with direct discrete-time pole placement for grid-tied converters with LCL filter," *IEEE Trans. Power Electron.*, vol. 32, no. 9, pp. 7207–7221, Sept. 2017.

[16] E. Wu and P. W. Lehn, "Digital current control of a voltage source converter with active damping of LCL resonance," *IEEE Trans. Power Electron.*, vol. 21, no. 5, pp. 1364–1373, Sept. 2006.

[17] V. Miskovic, V. Blasko, T. M. Jahns, A. H. C. Smith, and C. Romenesko, "Observer-based active damping of LCL resonance in grid-connected voltage source converters," *IEEE Trans. Ind. Appl.*, vol. 50, no. 6, pp. 3977–3985, Nov. 2014.

[18] G. F. Franklin, D. Powell, and M. L. Workman, *Digital Control of Dynamic Systems*, 3rd ed. Menlo Park, CA: Addison-Wesley, 1997.

[19] L. Zhang, L. Harnefors, and H. P. Nee, "Interconnection of two very weak AC systems by VSC-HVDC links using power-synchronization control," *IEEE Trans. Power Syst.*, vol. 26, no. 1, pp. 344–355, Feb. 2011.

[20] V. Kaura and V. Blasko, "Operation of a phase locked loop system under distorted utility conditions," *IEEE Trans. Ind. Appl.*, vol. 33, no. 1, pp. 58–63, Jan. 1997.